Chapter 5: $NiCo_2O_4$/NiO/rGO as non-precious metal-based electrode for supercapacitor application

5.1. Introduction

Accelerated rise of global population has led to rapid utilization of fossil fuel which is depleting over time. The greenhouse gas emissions from these fossil fuels are creating concerns as well. Renewable energy resources like wind, solar, etc. can be a substitute to these fossil fuels, however, their intermittency require efficient energy storage devices with high energy and power density. Among the electrochemical energy storage devices, supercapacitors are attracting attention due to their high power density, fast charging-discharging and long cycle life. Supercapacitors are inferior to batteries in terms of energy density. This can be mitigated by creating hybrid electrodes that combine electric double layer capacitance and pseudocapacitance into single electrode material [1]. As electrodes are the key driving agents of energy storage devices, the energy demand has intensified the search for efficient, cost-effective, and easily available electroactive materials. A growing amount of focus has been placed on synthesizing materials at the micro and nanoscale because the shape and dimensions of the materials are crucial in enhancing the electrochemical performance. Among the pseudocapacitive materials, transition metal oxides (TMOs) have high specific capacitance of around 100-2000 F/g, higher chemical stability than conducting polymers [2]. TMOs also possess higher energy density than carbon materials. Carbonaceous materials which provide electric double layer capacitance offer low energy density, thus limiting their performance. The single metallic oxide materials RuO_2 [3], Co_3O_4 [4], ZnO [5], and MnO_2 [6] are extensively studied supercapacitor electrodes. Co_3O_4 is a largely studied electroactive material which receives attention in supercapacitors due to its high theoretical capacitance of 3560 F/g [7], low cost, eco friendliness, strong chemical stability and multiple oxidation states which provide reversibility to the electrode [7, 8]. However, in real practice the high capacitance is not achieved due to several factors which reduce electron transport of Co_3O_4 such as low conductivity, particle aggregation, delayed kinetics, huge volume expansion and contraction [2]. Various morphologies of Co_3O_4 such as nanosheets [9], nanowires [10], nanoparticles [11], and nanofibers [12], etc. are studied as supercapacitor electrode. NiO is another promising pseudocapacitive material due to its availability,

affordability, high theoretical capacitance (2584 F/g), thermal and chemical stability [13, 14]. First reported porous NiO provides specific capacitance of 50-64 F/g [15]. The low electrical conductivity of NiO causes low electron transfer, which limits the performance of NiO supercapacitor. Thus, to boost its conductivity, NiO is composited with other materials such as graphene, carbon nanotubes, monovalent ion doping, different metal oxides, etc. Different morphologies of NiO namely nanoflakes [16], nanosheets [17], nanoflowers [18], nanospheres [19]. etc. are studied for supercapacitor [20]. On the other hand, mixed transition metal oxides possess higher conductivity and specific capacitance than the monometallic oxides due to the presence of two different metal cations exhibiting variable redox active sites. In the recent times, among the mixed metal oxides, spinel cobaltite [21] and metal molybdates [22] are promising candidates because of their low cost, availability and enhanced electrochemical activity. Low conductivity of monometallic oxides can be improved by these mixed transition metal oxides. Nickel cobaltite ($NiCo_2O_4$) is one of the potential candidates of the cobaltite family. As the microstructure of an electrode affects its electrochemical activity, therefore different morphologies and structures of $NiCo_2O_4$ are studied to improve its performance [23]. Although the conductivity of $NiCo_2O_4$ is higher than NiO and Co_3O_4, however, it is still not satisfactory as compared to the carbon-based materials. Incorporating it with higher conducting materials like graphene, carbon nanotubes, rGO, etc. one can increase its conductivity, rate capability, and cycling stability [24]. Carbon has garnered interest in energy storage systems due to its superior electrical conductivity, high electron mobility and mechanical strength. Its enormous surface area, high porosity, double layer charge storage mechanism and chemical inertness make it appropriate for applications requiring reliable energy storage. The drawbacks of both carbon and $NiCo_2O_4$ can be mitigated by combining them into composite system. For instance, $NiCo_2O_4$ when combined with single walled carbon nanotube (SWCNT) delivers specific capacitance of 1642 Fg^{-1} at 0.5 Ag^{-1}. The high performance of the nanocomposite comes from the synergistic contribution from each constituent material. The SWCNT provides electron and ion conducting channels whereas $NiCo_2O_4$ provides high capacitance [25].

In this chapter, a mixed metal oxide-based electrode material is developed and its supercapacitive performance is studied. $NiCo_2O_4$ is induced with NiO phase and combined with rGO nanosheets to create a hybrid supercapacitor electrode. Layer-on-layer morphology of $NiCo_2O_4$ with rGO nanosheets provide sufficient active sites for

capacitive performance. NiO phase in introduced to create additional redox sites to the nanocomposite. Thus, the pseudocapacitive materials $NiCo_2O_4$ and NiO offer high specific capacitance and energy density to the hybrid, whereas rGO nanosheets provide high cycling stability and power density to the hybrid. In other words, the nanocomposite $NiCo_2O_4$/NiO/rGO (CNOG) outperforms the pristine components due to the synergetic contribution from each.

The detailed morphological and structural characterizations of the nanocomposite CNOG are studied in chapter 3. In this chapter the electrochemical performance of CNOG as a supercapacitor electrode is studied. Symmetric supercapacitor performance of the developed CNOG is studied using aqueous as well as gel polymer electrolyte.

5.2 Experimental section

5.2.1 Electrochemical characterizations:

Electrochemical studies were conducted using three-electrode set up in Gamry (Model-Gamry Interface 1010 E) at ambient environment. The set-up of the three-electrode system is: Pt wire (counter electrode), Ag/AgCl (reference electrode) and graphite foil (1.5 × 1 cm^2) coated with prepared active material (working electrode). The catalyst slurry was prepared by mixing the active material: carbon black: nafion in 75: 15: 10 ratios in isopropanol and water. The working electrodes were prepared by coating the catalyst slurry on graphite foil. Prior to drop casting, graphite foils were washed with ethanol. Mass of active material deposited was calculated to be 0.1 mg. Cyclic voltammetry, Galvanostatic charge-discharge (GCD), and EIS were performed. The parameters were: - (-0.2 to 0.55) V window for CV, 3 M aqueous KOH solution was used as the electrolyte.

The specific capacitance (C_{sp}), energy density (E) and power density (P) of the symmetric supercapacitor are calculated by considering the following relations (equations 5.1-5.3).

$$C_{sp}\ (Fg^{-1}) = \frac{I\,\Delta t}{m\Delta V} \tag{5.1}$$

$$E\ (Whkg^{-1}) = \frac{1}{2} \times C_{cp} \times (\Delta V)^2 \times \frac{1000}{3600} \tag{5.2}$$

$$P\ (Wkg^{-1}) = \frac{E \times 3600}{\Delta t} \tag{5.3}$$

Where I is the discharge current in ampere, Δt is the discharging time in second, m is the mass of the active material (in gram) in both the positive and negative electrodes, ΔV is the potential window (in volt) [26, 27]. The specific capacitance of the single electrode (in three-electrode configuration) is measured using relation (5.1) where m is the mass of active mass in single electrode.

5.3 Results and Discussion

5.3.1 Electrochemical characterizations

5.3.1.1 Three-electrode electrochemical behaviour of the electrodes:

The electrochemical behaviours of the electrodes are studied by performing cyclic voltammetry using 3 M KOH as the optimized electrolyte. Cyclic voltammetry is performed in the potential window (-0.2 to 0.55) V vs. Ag/AgCl.

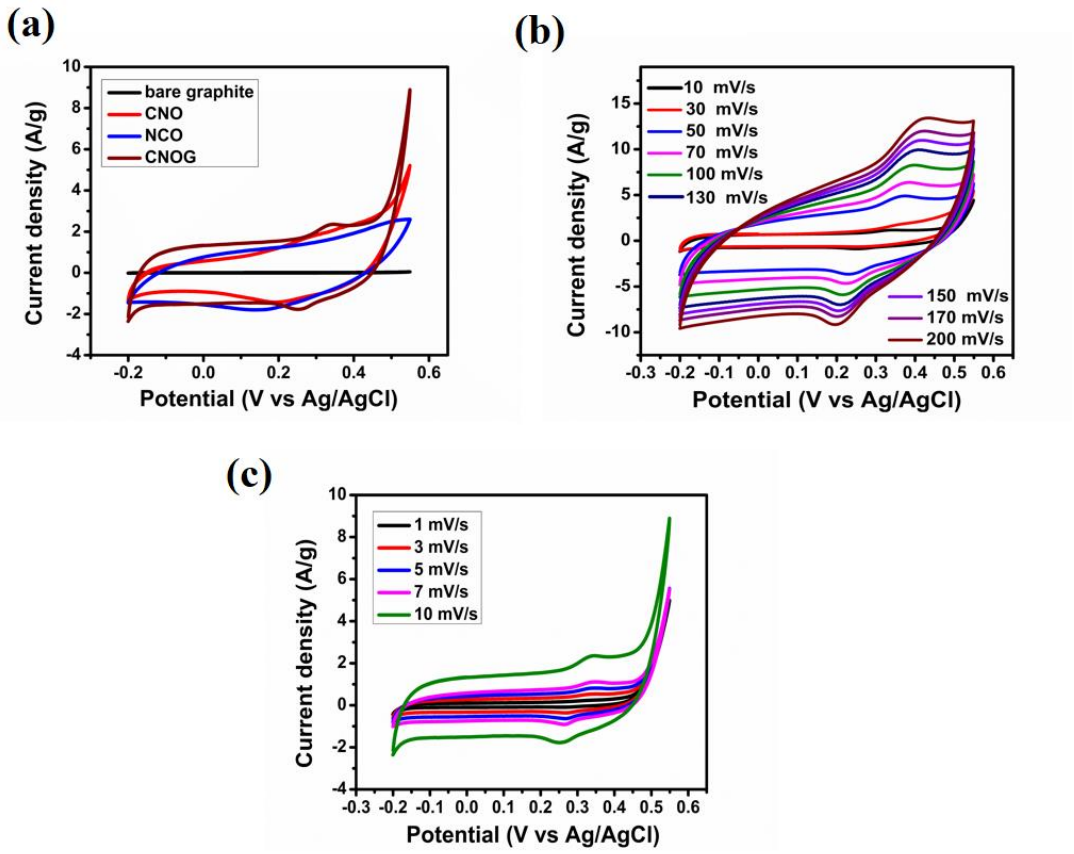

Figure 5.1: (a) Cyclic voltammetry in 3M KOH at 10 mV/s scan rate, Cyclic voltammetry of CNOG at (b) higher scan rate, (c) lower scan rate

As observed in fig. 5.1a, owing to the EDLC behaviour of reduced graphene oxide, CNOG offers higher integral surface area under CV than that of pristine NCO and CNO. Bare graphite foil shows negligible CV area and it does not exhibit any redox peak, which implies its inactiveness in charge storage. The redox reactions of Co and Ni in the redox couples Co_3O_4/CoOOH and NiO/NiOOH are responsible for the redox peaks [28]. The cyclic voltammogram of CNOG is displayed at both higher and lower scan rates in fig. 5.1b and 5.1c.

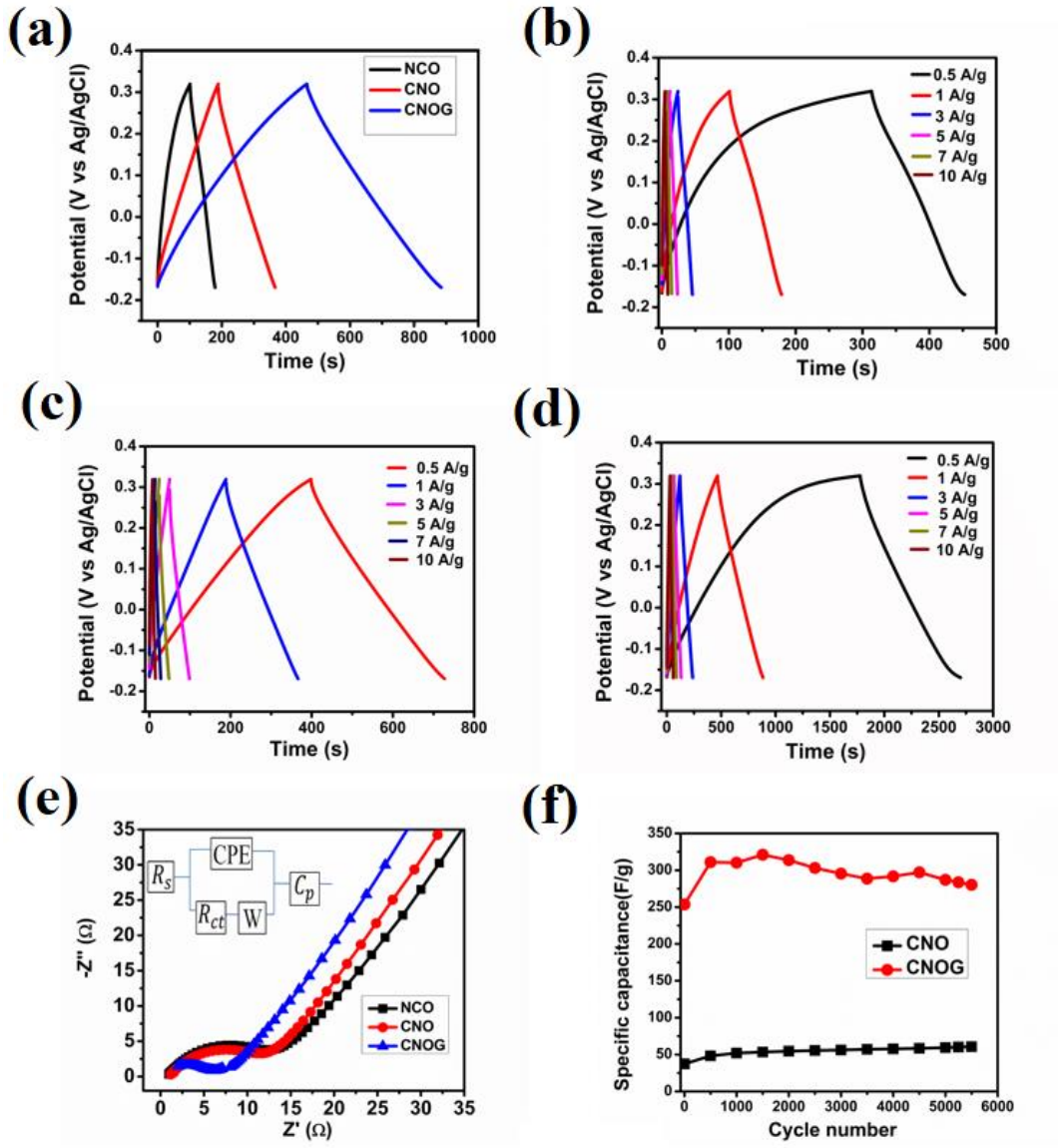

Figure 5.2: Galvanostatic charge-discharge (GCD) measurements of (a) NCO, CNO and CNOG at 1 A/g current density; (b) NCO, (c) CNO, and (d) CNOG from 0.5 to 10 A/g, (e) Nyquist plot of the electrodes (inset: equivalent circuit), (f) Cycling stability of CNOG and CNO at 10 A/g current density

The existence of pseudocapacitive component in CNOG is indicated by the strong redox peaks in the CV curve, which shows deviation from rectangular shape. Moreover, the shape of the cyclic voltammograms doesn't vary much with scan rate, which implies good reversibility of the electrode CNOG. The galvanostatic charge-discharge curve of each electrode at a current density of 1 A/g is shown in Figure 5.2a. CNOG exhibits the highest specific capacitance value of 854.94 F/g, whereas CNO exhibits 361.69 F/g. NCO has the lowest discharge time and lowest specific capacitance of 158.62 F/g at 1 A/g current density. At 10-fold current density, the specific capacitance of NCO, CNO, and CNOG becomes 86, 150, and 588 F/g respectively. The Coulombic efficiencies of NCO, CNO, and CNOG are 92.96%, 95.47%, and 96.75% respectively at 10 A/g current density. Figures 5.2b, 5.2c, and 5.2d display the GCDs of NCO, CNO, and CNOG at various current densities, ranging from 0.5 to 10 A/g. The presence of NiO in the binary composite CNO offers more electroactive sites, which increases faradaic reactions, thereby enhancing the specific capacitance. Moreover, by adding NiO, impurity band effects are introduced, which enhances electronic conductivity and facilitates efficient charge transfer. The addition of rGO provides EDLC contribution to the hybrid electrode, which makes the GCD almost linear in shape. The porous rGO nanosheets enable easy penetration of electrolyte ions into the electrode surface. The metal oxides $NiCo_2O_4$ and NiO embedded on rGO nanosheets reduce the restacking of the rGO nanosheets, leading to availability of more active sites. This synergistic contribution causes a drastic increase in specific capacitance of the hybrid CNOG. Figure 5.2e displays the Nyquist plots of the electrode in 3 M KOH. The comparable electrochemical electrical circuit that best fits the experimental results is shown in the inset of figure 5.2e. The different processes and their related impedances are reflected as different elements in the circuit. The elements are: series resistance (R_s), charge transfer resistance (R_{ct}), constant phase element (CPE) representing the electric double layer capacitance, faradaic capacitance (C_p), and Warburg impedance (W). The R_s values of NCO, CNO and CNOG are found to be 0.86 Ω, 1.073 Ω, and 15.10 μΩ respectively. Such low series resistance of CNOG suggests negligible inter-particle resistance and contact resistance offered by the electrode. Additionally, CNOG has a lower R_{ct} value (6.219 Ω) than NCO (12.25 Ω) and CNO (10.08 Ω). The nearly vertical line in the lower frequency region represents the Warburg impedance. Lower Warburg impedance implies more effortless diffusion of electrolyte ions into the electrode's active sites [29]. In this study nearly vertical line of

CNOG indicates good capacitive behaviour. It offers W value 0.005374 $Ss^{\frac{1}{2}}$, whereas NCO and CNO offer 0.01081 and 0.008691 $Ss^{\frac{1}{2}}$ respectively. Thus, CNOG provide excellent conductivity, fast electrolyte ion diffusion and electrode-electrolyte interaction. Hence, these enhanced properties make CNOG a promising supercapacitor electrode. The high surface area of rGO, proper utilisation of the surface due to reduced stacking of these nanosheets lead to the least charge transfer resistance of CNOG. Cycling stability has been performed for CNO and CNOG to assess the durability of the electrode for 5500 GCD cycles recorded at 10 A/g current density in 3 M KOH aqueous solution. It is observed from fig. 5.2f that with increase in cycle number the specific capacitance of CNOG slightly increases and reaches its maximum at 1500th cycle from 253.67 (1st cycle) to 321.05 F/g, which may be due to activation of the electrode after continuous insertion and withdrawal of K^+ ions during the charging-discharging process [30]. This increase in capacitance may be due to dissolution and redistribution of the metal oxides $NiCo_2O_4$ and NiO and formation of symmetrical nanoplatelets (namely hexagonal, pentagonal, etc.), as observed in fig. 5.3a [31]. This variation of geometry of the nanoplatelets may affect the cycling stability in the long run as pentagonal platelets may develop internal strain causing cracks, defects and mechanical instability in the system. On the other hand, rGO nanosheets are seen intact even after 5500 cycles as shown in fig. 5.3b. After prolonged charging-discharging, the charge transfer resistance reduces (4.985 **Ω**, as displayed in fig. 5.3c), thus facilitating more electrolyte ions to penetrate into the electrode [32]. After 1500 cycles, the specific capacitance reduces and at the end of 5500th cycle, its value becomes 280.16 F/g, which is 87.26% of that of 1500th cycle. CNOG offers coulombic efficiency of 99.10% after 5500th cycle. Cycling stability of CNO has been performed for comparison. It is observed that in case of CNO the specific capacitance keeps on increasing from 1st cycle (37.3 F/g) to the last cycle (60.5 F/g). Coulombic efficiency of 99.3% is obtained for CNO. This continuous increase in capacitance may be due to structural stabilization of the active material [30, 31, 33]. Due to the pseudocapacitive components $NiCo_2O_4$ and NiO, CNO exhibits structural instability, because of the on-going faradaic reactions during charge-discharge process. During continuous charge-discharge, the material may undergo various transformations which leads to creation of more surface active sites, which increases the electrode-electrolyte interactions. Thus, the enhanced effective surface area for ion adsorption leads

to enhanced capacitance [34]. On the other hand, high structural and cycling stability of CNOG arises due to the presence of EDLC component rGO. The layer-on-layer structure of CNOG ensures proper utilization of the surface area and minimises restacking and agglomeration.

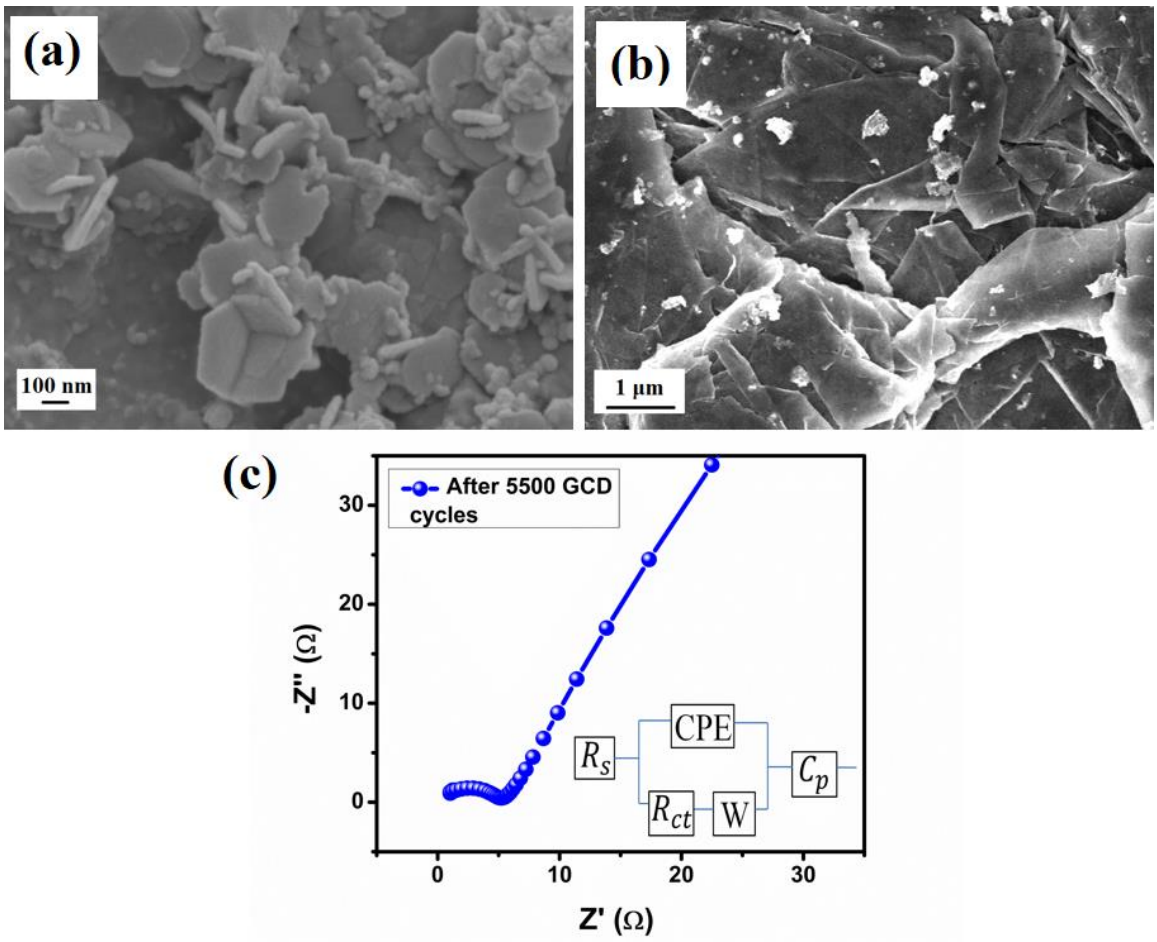

Figure 5.3: Post cycling stability test of CNOG: (a), (b) FESEM images at different magnifications, (c) EIS (Inset: Equivalent circuit)

5.3.1.2 Electrochemical behaviour of the symmetric supercapacitor:

5.3.1.2.1 3M KOH aqueous electrolyte:

To understand the practical application of CNOG as supercapacitor, a symmetric supercapacitor CNOG//CNOG is developed using CNOG as positive and negative electrode, and its behaviour is studied in 3 M KOH as the electrolyte using two-electrode arrangement. To determine the optimum potential window, cyclic voltammetry is

performed at 10 mV/s scan rate at various potential windows as displayed in fig. 5.4a. Figure 5.4a shows that the current increases rapidly at potentials higher than 0.9 V (vs. Ag/AgCl). This is mostly because of the oxygen evolution process that results from the splitting of the aqueous KOH electrolyte. The CV of 0.85 V and 0.90 V looks good without any sharp increase in current.

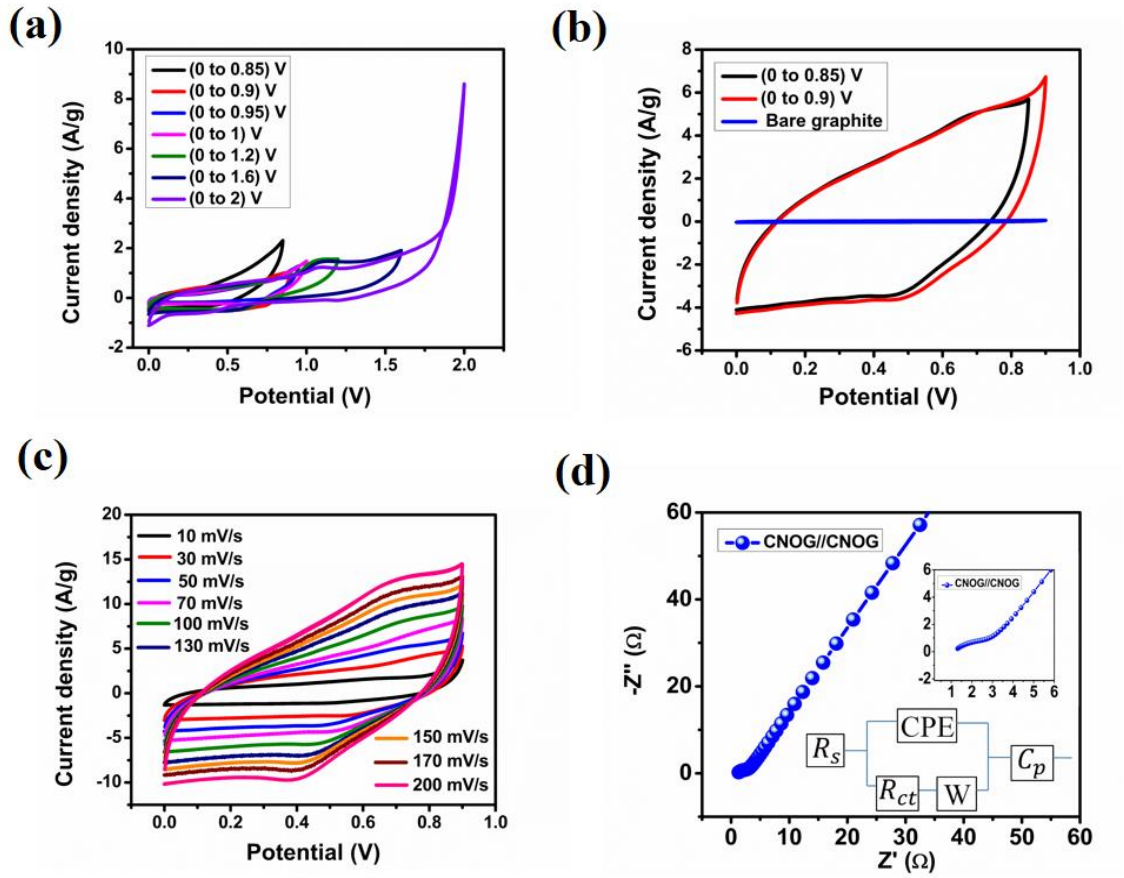

Figure 5.4: Electrochemical study of symmetric supercapacitor CNOG//CNOG in 3M KOH aqueous electrolyte: (a) Cyclic voltammogram of different potential windows, (b) Comparing windows 0.85 V, 0.90 V and bare graphite at 50 mV/s, (c) Cyclic voltammogram in (0 to 0.9) V window at varying scan rate, (d) Nyquist plot. (Top inset: magnified view of higher frequency Nyquist plot, bottom inset: equivalent circuit)

To find the optimum window, the CV areas of 0.85 and 0.9 V are compared in fig. 5.4b and it is observed that 0.90 V exhibits higher CV area, which gives more areal capacitance than 0.85 V. Thus, 0.90 V is found to the optimum potential window without any side reactions. The shapes of the CVs shown in fig. 5.4c, are quasi-rectangular, which is attributed to the presence of EDLC (rGO) and pseudocapacitance (CNO) storage in the

system. Consistency of the CV shape at higher scan rate indicates good reversibility of the symmetric supercapacitor CNOG//CNOG. The symmetric supercapacitor offers excellent conductivity as can be inferred from the Nyquist plot shown in fig. 5.4d. An electrical circuit fitting the results is shown in inset of fig. 5.4d, which gives R_s and R_{ct} to be 1.246 Ω and 0.739 Ω respectively. The nearly vertical line in the lower frequency region with Warburg impedance 0.007831 $Ss^{\frac{1}{2}}$ implies fast electron and ion diffusion into the electrode. Thus, the synergistic contribution of the highly conducting rGO nanosheets, redox active sites of pseudocapacitive $NiCo_2O_4$ and NiO, interfacial interaction endowed by layer-on-layer structure, and mesoporous nature bestows the hybrid CNOG with enhanced capacitive behaviour.

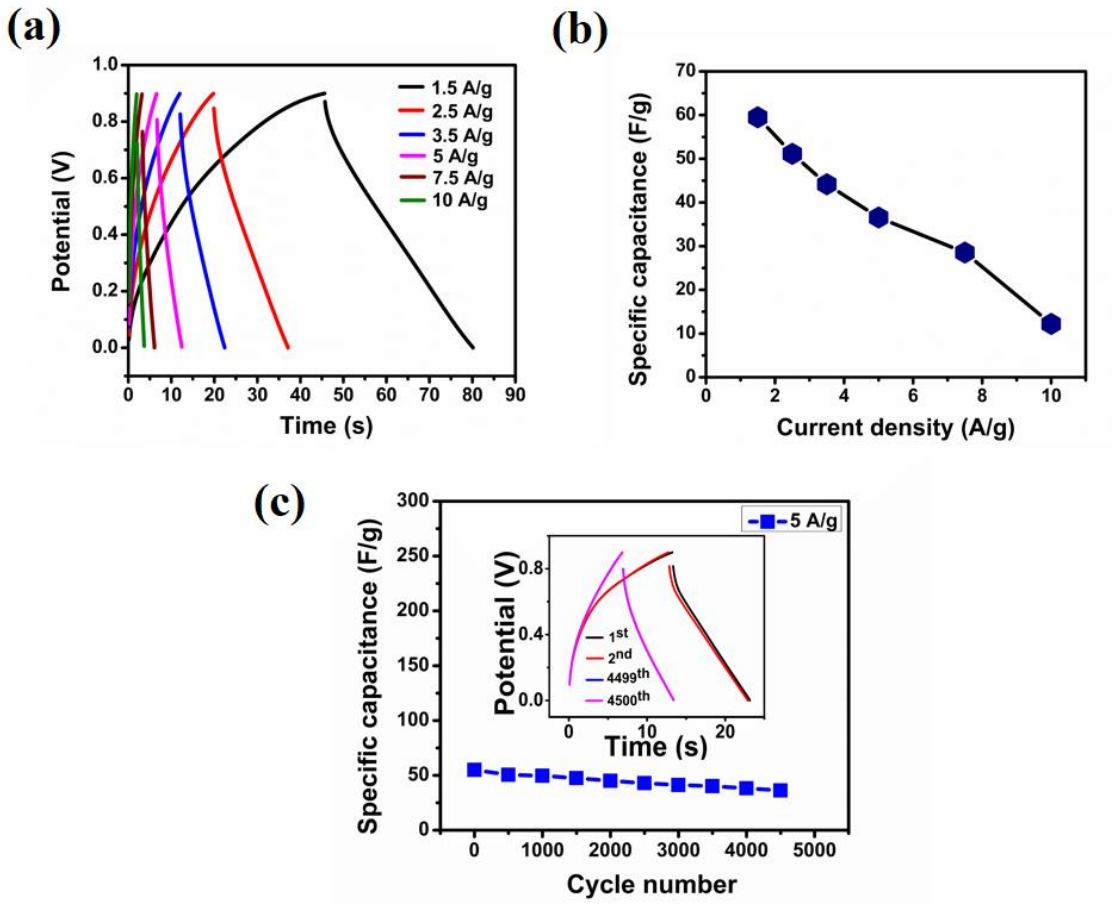

Figure 5.5: Electrochemical study of symmetric supercapacitor CNOG//CNOG in 3M KOH aqueous electrolyte: (a) GCD at varying current densities, (b) Specific capacitance vs. current density plot, (c) Specific capacitance up to 4500 GCD cycles (Inset: First two and last two cycles)

GCD is performed at current densities varying from 1.5 A/g to 10 A/g. The GCD curves (in fig. 5.5a) corroborate well with the CV curves, establishing the presence of EDLC and pseudocapacitance in the symmetric supercapacitor. At 1.5 A/g current density, specific capacitance of 59.49 F/g and energy, power density of 6.69 Wh/kg and 698 W/kg respectively, are obtained. At higher current density, the specific capacitance reduces due to lesser diffusion of electrolyte ions. The specific capacitance versus current density plot shown in fig. 5.5b shows capacitance retention of 61.44% at 5 A/g and 20.5% at 10 A/g current density, maintaining 90.37% coulombic efficiency at 10 A/g current density. The inferior rate-capability of the symmetric device is basically because of sluggish reactions due to limitation in ion diffusion kinetics at higher current density. At higher current density, all the available active sites cannot be reached as the electrolyte ions find difficulty in diffusion and penetration into the pores of the material. The redox active sites do not get enough time to initiate the electrochemical reactions. Only the active sites exposed to the surface participate in charge storage mechanism. Thus, at higher current density the ion diffusion and EDLC formation gets constrained only to the outer surface of the electrode [35, 36]. Since all the available redox active sites do not contribute to the capacitance of the device, it leads to reduced specific capacitance of the symmetric device at higher current density. In order to examine retention during continuous charge-discharge, cycling stability is carried out for 4500 GCD cycles, as seen in fig. 5.5c. The symmetric supercapacitor CNOG//CNOG offers specific capacitance of 55 F/g in the first cycle, which reduces to 50.3 F/g in the 500^{th} cycle. After 4500 cycles, specific capacitance of 36.25 F/g is obtained which shows a retention of 65.9%. In the first cycle, an energy density of 6.191 Wh/kg and a specific power value of 2249.75 W/kg are achieved. This energy density reduces to 4.0979 Wh/kg after 4500 GCD cycles. Coulombic efficiency which is 74.8053% in the first cycle increases to 95.57% in the 4500^{th} cycle.

To understand the structural changes in the electrode after 4500 charge-discharge cycles of the symmetric supercapacitor, and to reveal the formation of any new phase, XRD is performed. The diffraction peaks of the active material (fig. 5.6a) are not visible due to the intense graphite foil (substrate used) peaks at 26° and 53.9° corresponding to (002) and (004) plane (JCPDS no. 75-2078) (as shown in fig. 5.6b).

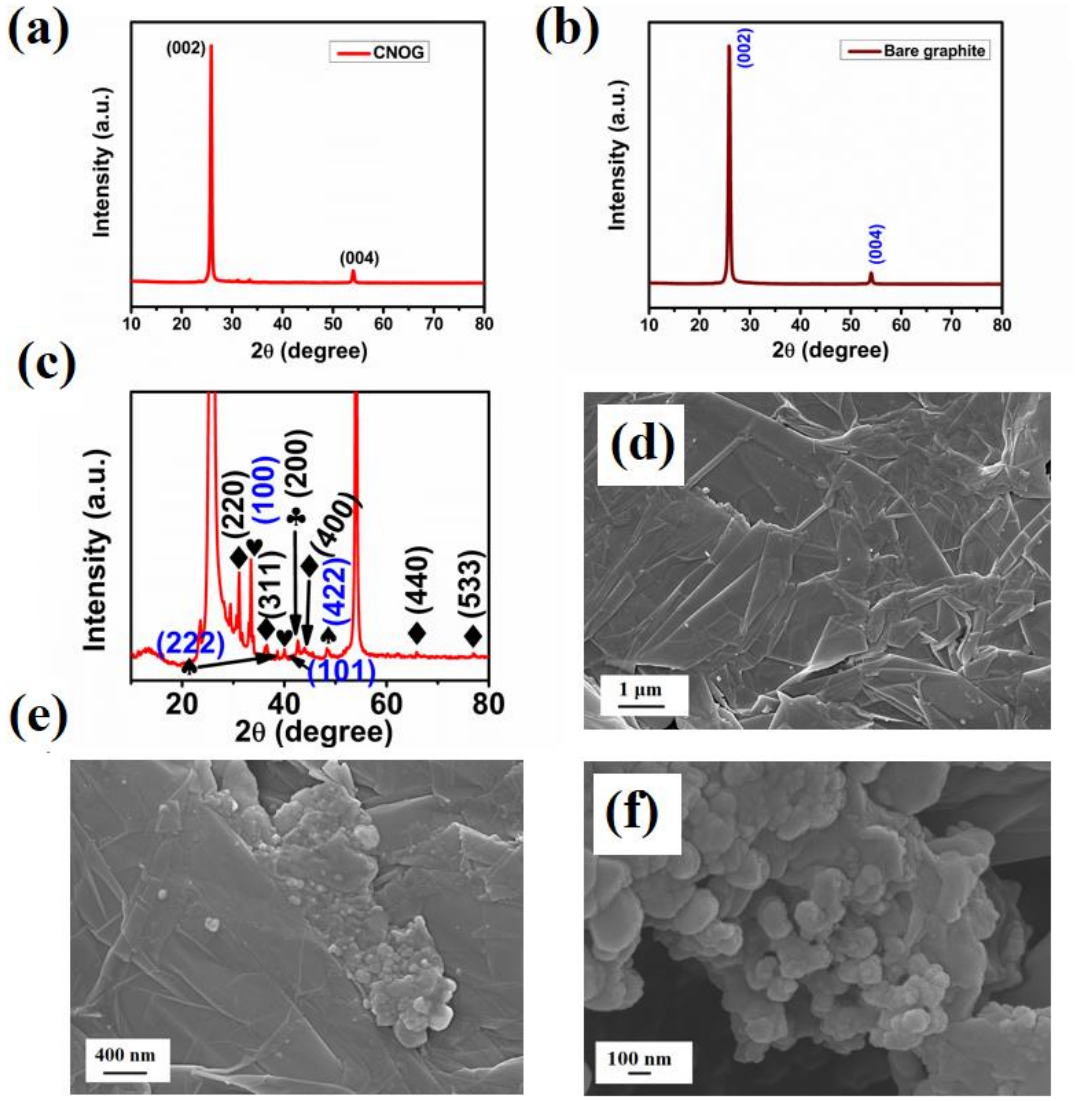

Figure 5.6: Structural and morphological characterizations after cycling stability of the symmetric supercapacitor electrode: (a) XRD pattern of CNOG, (b) XRD of bare graphite, (c) Magnified view of XRD peaks of active material; with symbols signifying: ♠ Co_2O_4 ♣ NiO ♥ $Ni(OH)_2$ ♦ $NiCo_2O_4$ phase), (d)-(f) FESEM images

However, on magnifying the XRD pattern, the peaks of the active material are clearly visible (as shown in fig. 5.6c). The peaks at 31.3°, 36.5°, 44°, 65.8°, and 77° are of (220), (311), (400), (440), and (533) planes of $NiCo_2O_4$. Only one diffraction peak of NiO is found at 42.6° corresponding to (200) plane. Disappearance of the other peaks suggest the diminishing of the NiO phase and formation of different phase during the redox reactions taking place during the charge storage process. Additional peaks which are observed at 33.3°, and 40° reveal the formation of new phase $Ni(OH)_2$ (JCPDS 38-0715).

These peaks are attributed to (100), (101) plane of $Ni(OH)_2$ [37]. The formation reaction of $Ni(OH)_2$ can be written as $NiO + OH^- \rightleftharpoons NiOOH + e^-$ and $NiOOH + H_2O + e^- \rightleftharpoons Ni(OH)_2 + OH^-$. The peaks at 38.6° and 48.4° are due to the (222) and (422) plane of Co_2O_4 (JCPDS 9-418) [38]. This Co_2O_4 may be formed due to the breaking down of $NiCo_2O_4$ according to the equation $NiO + Co_2O_4 \rightleftharpoons NiCo_2O_4$. The XRD peaks of $Ni(OH)_2$ and Co_2O_4 are found only for certain specific planes, which may be due to some preferential directional growth during the charging-discharging process. The morphological changes of the electrode are studied by observing the FESEM images. It is observed from fig. 5.6d, the restacking of $NiCo_2O_4$ nanoflakes and the wrinkled structure of rGO nanosheets. From fig. 5.6e and 5.6f, the agglomeration of NiO nanoparticles is evident. Thus, after such agglomeration and restacking, the interfacial interactions among the individual components, the active surface area and the redox active sites reduces, which leads to reduced specific capacitance of the symmetric device, which is corroborating well with fig. 5.5c.

5.3.1.2.2 PVA/3M KOH gel polymer electrolyte:

The potential window of symmetric supercapacitor CNOG//CNOG cannot be increased beyond 0.9 V in aqueous 3 M KOH electrolyte because of water splitting taking place. To obtain a higher window, hydrogel polymer electrolyte of PVA/3 M KOH is developed. The CV curves of the symmetric supercapacitor in PVA/3 M KOH for various potential windows are displayed in Figure 5.7a. It has been observed that side reactions occurring on the electrodes cause the current to surge dramatically over 1.3 V. Therefore, 1.3 V is considered to be the optimum window for the hydrogel polymer electrolyte. As the CV curves retain their shape at higher scan rates, the symmetric supercapacitor demonstrates its reversibility at higher scans as shown in fig. 5.7b. GCD is carried out in the window (0 to 1.3) V by varying the current densities from 1.5 to 10 A/g, as seen in fig. 5.7c. Non-linear GCD curves implies the presence of both EDLC and pseudocapacitance in the electrode. Specific capacitance of 88.80 F/g along with energy, power density being 20.84 Wh/kg and 1003.2 W/kg respectively are obtained at 1.5 A/g current density. At 10 A/g, specific capacitance obtained is 32.63 F/g with capacitance retention of 36.75% (presented in specific capacitance versus current density plot in fig. 5.7d). A comparison between this study and other reported works is made using the Ragone plot shown in fig. 5.7e. It is found that CNOG//CNOG using PVA/ 3 M KOH offers higher energy and

power density than many other symmetric supercapacitors [39-48]. Thus, CNOG can be a potential supercapacitor working at high current density.

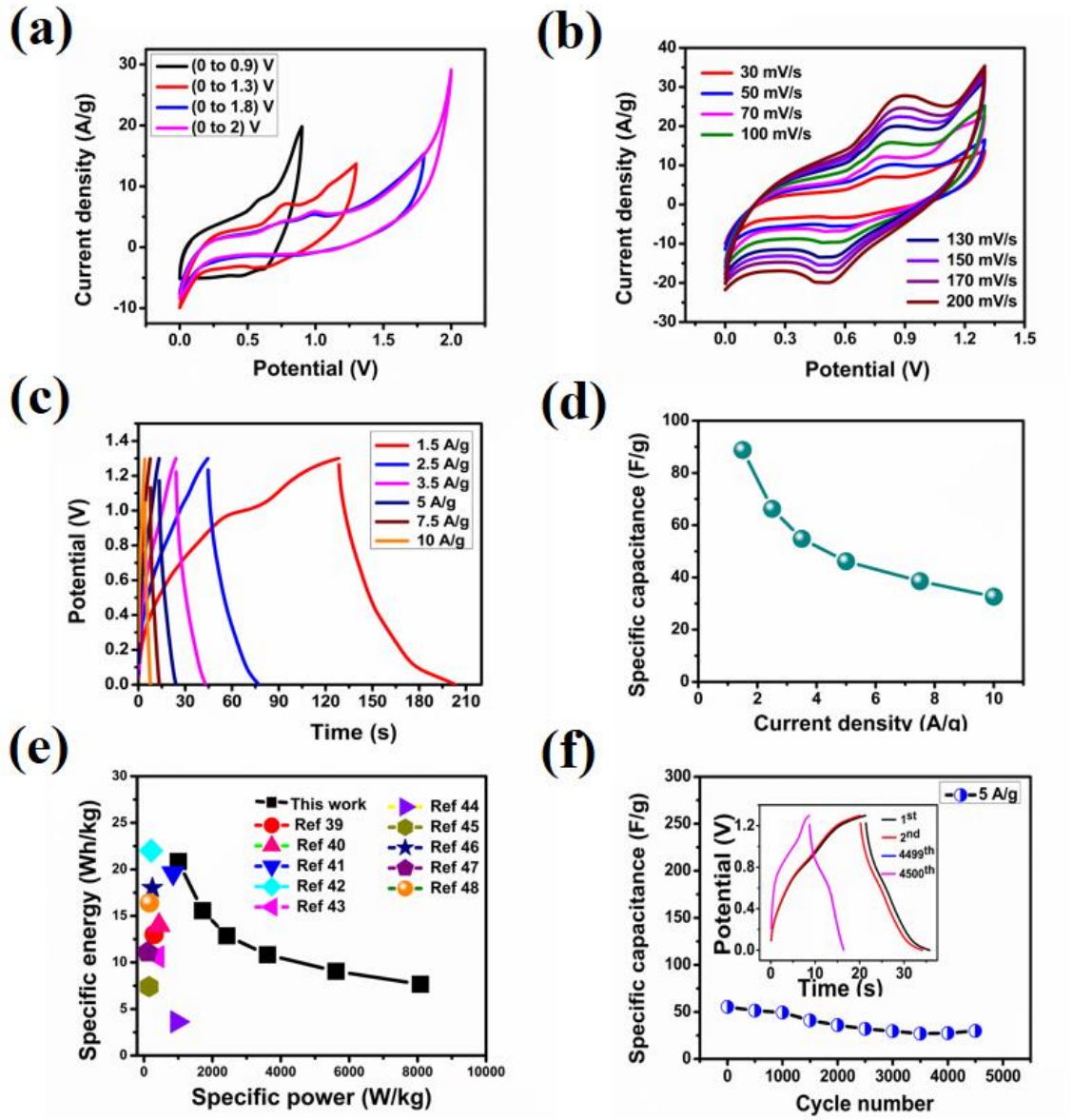

Figure 5.7: Two-electrode electrochemical characterization of symmetric supercapacitor CNOG//CNOG in hydrogel polymer electrolyte PVA/3M KOH: (a) Cyclic voltammetry in different potential window, (b) Cyclic voltammograms in (0 to 1.3) V with varying scan rate, (c) Galvanostatic charge-discharge curves at varying current density, (d) Specific capacitance vs. current density plot, (e) Ragone plot, (f) Specific capacitance with cycle number (Inset: First two and last two cycles)

The cycling stability of CNOG//CNOG over 4500 GCD cycles (shown in fig. 5.7f) demonstrates that, beyond 2500 cycles, the specific capacitance nearly stays constant, retaining 57.5% and 54.10% capacitance at the 2500^{th} and 4500^{th} cycles, respectively, maintaining 90.23% of the coulombic efficiency after 4500^{th} cycle. Thus, the mesoporous morphology, interfacial interaction among $NiCo_2O_4$ nanoflakes, NiO nanoparticles and rGO nanosheets, increased conductivity and surface area of CNOG allows more ion movement and penetration into the electrode, further increasing its capacitance and energy density.

To validate the practical application of the assembled hydrogel based symmetric supercapacitor cell, 1.8 V LED light has been glowed. It is observed that 2 cells in series can glow a 1.8 V LED. However, 4 cells in series can glow the LED with more intensity and higher time (~25 to 30 seconds). The images of cells connected in series along with the lit LED are shown in fig. 5.8a and 5.8b respectively.

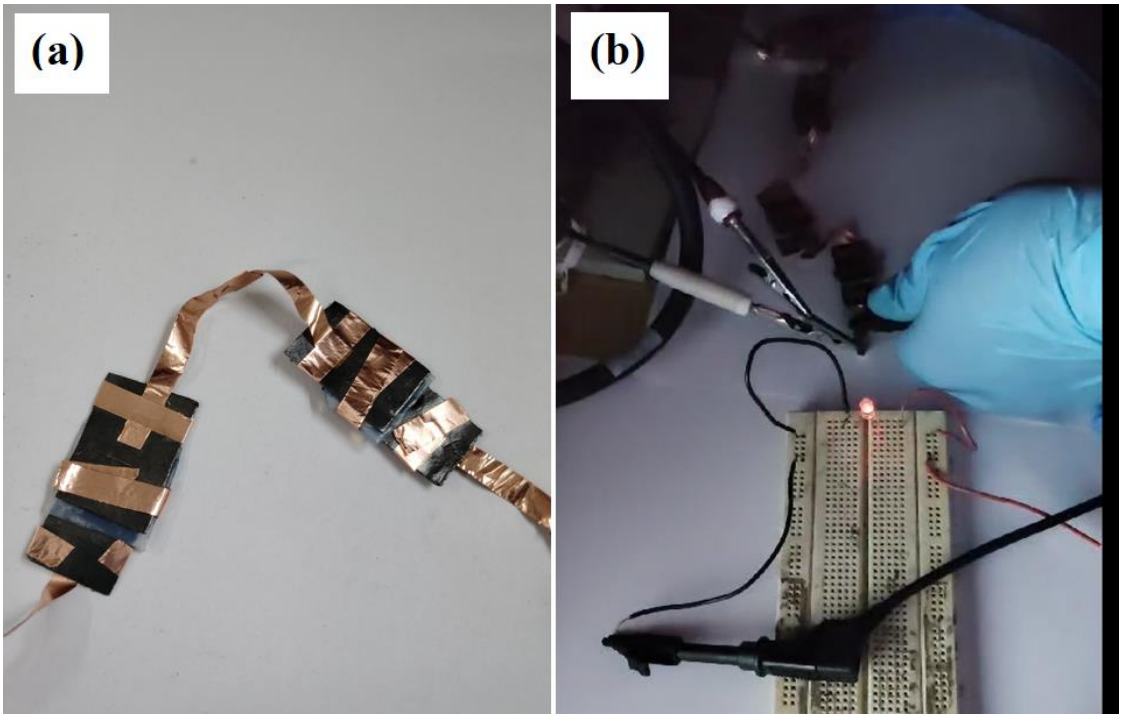

Figure 5.8: (a) 2 CNOG//CNOG cells in series, (b) 1.8 V LED glow with 4 cells in series

5.4 Conclusion

In summary, this chapter contains the electrochemical characterizations of the developed nanocomposite $NiCo_2O_4$/NiO/rGO (CNOG) as supercapacitor electrode. The presence of variable oxidation states of Ni and Co, and the presence of mesopores result in enhanced capacitance of the electrode CNOG. Higher specific capacitance of 855 F/g is obtained for the hybrid electrode which benefits from the synergistic contribution of the two-dimensional nanoflakes of $NiCo_2O_4$, conducting rGO nanosheets and NiO nanoparticles. The reduced stability of CNO due to the presence of the pseudocapacitive components $NiCo_2O_4$ and NiO, is compensated by the presence of rGO nanosheets. On the other hand, the pseudocapacitive components $NiCo_2O_4$ and NiO impart high capacitance to the nanocomposite CNOG. The mesopores present on the nanocomposite CNOG increases the electrode-electrolyte interactions and decreases ion transfer pathways. rGO reduces the agglomeration of the transition metal oxides, which on the other hand reduces the restacking of rGO nanosheets. The symmetric supercapacitor CNOG//CNOG in aqueous 3 M KOH offers a specific capacitance of 59.48 F/g at 1.5 A/g, and specific energy and power of 6.69 Wh/kg and 698 W/kg respectively. The symmetric supercapacitor maintains 90.37% Coulombic efficiency at 10 A/g current density while displaying capacitance retention of 61.44% at 5 A/g and 20.5% at 10 A/g current density. In contrast, the symmetric supercapacitor CNOG//CNOG in gel polymer electrolyte outshines by offering specific capacitance of 88.8 F/g, energy and power density being 20.84 Wh/kg and 1003 W/kg respectively at 1.5 A/g. At higher current density of 10 A/g, specific capacitance of 32.63 F/g is obtained. Four such cells in series can glow a 1.8 V light-emitting diode for around 30 seconds. Thus, CNOG offers good performance as a supercapacitor electrode.

5.5 References:

1. Bhattacharya, K., Deb, P. Hybrid nanostructured C-dot decorated Fe_3O_4 electrode materials for superior electrochemical energy storage performance. *Dalton Trans*. 44 (19):9221-9229, 2015.
2. Liang, R., Du, Y., Xiao, P., Cheng, J., Yuan, S., Chen, Y., Yuan, J. and Chen, J. Transition metal oxide electrode materials for supercapacitors: a review of recent developments. *Nanomaterials*, 11 (5):1248, 2021.

3. Majumdar, D., Maiyalagan, T. and Jiang, Z. Recent progress in ruthenium oxide-based composites for supercapacitor applications. *ChemElectroChem*, 6 (17):4343-4372, 2019.
4. Hu, X., Wei, L., Chen, R., Wu, Q. and Li, J. Reviews and Prospectives of Co_3O_4-Based Nanomaterials for Supercapacitor Application. *ChemistrySelect*, 5 (17):5268-5288, 2020.
5. Theerthagiri, J., Salla, S., Senthil, R.A., Nithyadharseni, P., Madankumar, A., Arunachalam, P., Maiyalagan, T. and Kim, H.S. A review on ZnO nanostructured materials: energy, environmental and biological applications. *Nanotechnology*, 30 (39):92001, 2019.
6. Wang, J.G., Kang, F. and Wei, B. Engineering of MnO_2-based nanocomposites for high-performance supercapacitors. *Progress in Materials Science*, *74*:51-124, 2015.
7. Meng, T., Xu, Q.Q., Wang, Z.H., Li, Y.T., Gao, Z.M., Xing, X.Y. and Ren, T.Z. Co_3O_4 nanorods with self-assembled nanoparticles in queue for supercapacitor. *Electrochimica Acta*, 180:104-111, 2015.
8. Jia, W., Li, J., Lu, Z., Juan, Y. and Jiang, Y. Synthesis of Honeycomb-like Co_3O_4 Nanosheets with Excellent Supercapacitive Performance by morphological controlling derived from the alkaline source ratio. *Materials*, *11* (9):1560, 2018.
9. Yang, Q., Lu, Z., Sun, X. and Liu, J. Ultrathin Co_3O_4 nanosheet arrays with high supercapacitive performance. *Scientific Reports*, 3 (1):3537, 2013.
10. Xia, X.H., Tu, J.P., Mai, Y.J., Wang, X.L., Gu, C.D. and Zhao, X.B. Self-supported hydrothermal synthesized hollow Co_3O_4 nanowire arrays with high supercapacitor capacitance. *Journal of Materials Chemistry*, 21 (25):9319-9325, 2011.
11. Zallouz, S., Réty, B., Vidal, L., Le Meins, J.M. and Matei Ghimbeu, C. Co_3O_4 nanoparticles embedded in mesoporous carbon for supercapacitor applications. *ACS Applied Nano Materials*, 4 (5):5022-5037, 2021.
12. Kumar, M., Subramania, A. and Balakrishnan, K. Preparation of electrospun Co_3O_4 nanofibers as electrode material for high performance asymmetric supercapacitors. *Electrochimica Acta*, 149:152-158, 2014.
13. Kate, R.S., Khalate, S.A. and Deokate, R.J. Overview of nanostructured metal oxides and pure nickel oxide (NiO) electrodes for supercapacitors: A review. *Journal of Alloys and Compounds*, 734:89-111, 2018.

14. Jayakumar, S., Santhosh, P.C., Mohideen, M.M. and Radhamani, A.V. A comprehensive review of metal oxides (RuO_2, Co_3O_4, MnO_2 and NiO) for supercapacitor applications and global market trends. *Journal of Alloys and Compounds*, 976:173170, 2023.
15. Liu, K.C. and Anderson, M.A. Porous nickel oxide/nickel films for electrochemical capacitors. *Journal of the Electrochemical Society*, 143 (1):124, 1996.
16. Vijayakumar, S., Nagamuthu, S. and Muralidharan, G. Supercapacitor studies on NiO nanoflakes synthesized through a microwave route. *ACS applied materials & interfaces*, 5 (6):2188-2196, 2013.
17. Xiao, H., Yao, S., Liu, H., Qu, F., Zhang, X. and Wu, X. NiO nanosheet assembles for supercapacitor electrode materials. *Progress in Natural Science: Materials International*, 26 (3):271-275, 2016.
18. Du, D., Hu, Z., Liu, Y., Deng, Y. and Liu, J. Preparation and characterization of flower-like microspheres of nano-NiO as electrode material for supercapacitor. *Journal of alloys and compounds*, 589:82-87, 2014.
19. Sun, W., Chen, L., Meng, S., Wang, Y., Li, H., Han, Y. and Wei, N. Synthesis of NiO nanospheres with ultrasonic method for supercapacitors. *Materials science in semiconductor processing*, 17:129-133, 2014.
20. Paulose, R., Mohan, R. and Parihar, V. Nanostructured nickel oxide and its electrochemical behaviour—A brief review. *Nano-Structures & Nano-Objects*, 11:102-111, 2017.
21. Chang, S.K., Zainal, Z., Tan, K.B., Yusof, N.A., Yusoff, W.M.D.W. and Prabaharan, S.R.S. Recent development in spinel cobaltites for supercapacitor application. *Ceramics International*, 41 (1):1-14, 2015.
22. Gurusamy, L., Karuppasamy, L., Anandan, S., Liu, C.H. and Wu, J.J. Recent advances on metal molybdate-based electrode materials for supercapacitor application. *Journal of Energy Storage*, 79:110122, 2024.
23. Dubal, D.P., Gomez-Romero, P., Sankapal, B.R. and Holze, R. Nickel cobaltite as an emerging material for supercapacitors: an overview. *Nano Energy*, 11:377-399, 2015.
24. Mahadik, S.M., Chodankar, N.R., Han, Y.K., Dubal, D.P. and Patil, S. Nickel cobaltite: A positive electrode material for hybrid supercapacitors. *ChemSusChem*, 14 (24):5384-5398, 2021.

25. Cui, B., Lin, H., Li, J.B., Li, X., Yang, J. and Tao, J. Core–ring structured $NiCo_2O_4$ nanoplatelets: synthesis, characterization, and electrocatalytic applications. *Advanced Functional Materials*, 18 (9):1440-1447, 2008.
26. Ghosh, K., Yue, C.Y., Sk, M.M., Jena, R.K. and Bi, S. Development of a 3D graphene aerogel and 3D porous graphene/MnO_2@ polyaniline hybrid film for all-solid-state flexible asymmetric supercapacitors. *Sustainable Energy & Fuels*, 2 (1):280-293, 2018.
27. Shukla, P.S., Agrawal, A., Gaur, A. and Varma, G.D. Synthesis of mesoporous Zn-doped $MnCo_2O_4$ nanoparticles for high-energy density solid-state asymmetric supercapacitor. *Journal of Energy Storage*, 73:109229, 2023.
28. Askari, M.B. and Salarizadeh, P. Superior catalytic performance of $NiCo_2O_4$ nanorods loaded rGO towards methanol electro-oxidation and hydrogen evolution reaction. *Journal of Molecular Liquids, 291*:111306, 2019.
29. Chaudhari, S., Bhattacharjya, D. and Yu, J.S. 1-Dimensional porous α-Fe_2O_3 nanorods as high performance electrode material for supercapacitors. *RSC Advances*, 3 (47):25120-25128, 2013.
30. Xia, H., Meng, Y.S., Li, X., Yuan, G. and Cui, C. Porous manganese oxide generated from lithiation/delithiation with improved electrochemical oxidation for supercapacitors. *J. Mater. Chem.*, 21 (39):15521-15526, 2011.
31. Qiao, Z., Yang, X., Yang, S., Zhang, L. and Cao, B. 3D hierarchical MnO_2 nanorod/welded Ag-nanowire-network composites for high-performance supercapacitor electrodes. *Chemical communications*, 52 (51):7998-8001, 2016.
32. Sridhar, D., Meunier, J.L. and Omanovic, S. Directly grown carbon nano-fibers on nickel foam as binder-free long-lasting supercapacitor electrodes. *Materials Chemistry and Physics*, 223:434-440, 2019.
33. Athouël, L., Moser, F., Dugas, R., Crosnier, O., Bélanger, D. and Brousse, T. Variation of the MnO_2 birnessite structure upon charge/discharge in an electrochemical supercapacitor electrode in aqueous Na_2SO_4 electrolyte. J. *Phys. Chem. C*, 112(18):7270-7277, 2008.
34. Aziz, S.B., Brza, M.A., Abdulwahid, R.T., Hassan, J., Tahir, H.B., Al-Saeedi, S.I., Abdullah, R.M. and Hadi, J.M. Electrochemical properties of a novel EDLC derived from plasticized biopolymer based electrolytes with valuable energy density close to NiMH batteries. Scientific Reports, 13(1):21139, 2023.

35. Gunday, S.T., Cevik, E., Anil, I., Alagha, O. and Bozkurt, A. High-temperature symmetric supercapacitor applications of anhydrous gel electrolytes including doped triazole terminated flexible spacers. *Journal of Molecular Liquids*, 301:112400, 2020.
36. Shah, S.S., Cevik, E., Aziz, M.A., Qahtan, T.F., Bozkurt, A. and Yamani, Z.H. Jute sticks derived and commercially available activated carbons for symmetric supercapacitors with bio-electrolyte: a comparative study. *Synthetic Metals*, 277:116765, 2021.
37. Rathore, D., Sharma, M.D., Sharma, A., Basu, M. and Pande, S. Aggregates of Ni/$Ni(OH)_2$/NiOOH nanoworms on carbon cloth for electrocatalytic hydrogen evolution. *Langmuir*, 36(46):14019-14030, 2020.
38. Khan, M.I., Muhammad, N., Tariq, M., Nishan, U., Razaq, A., Saleh, T.A., Haija, M.A., Ismail, I. and Rahim, A. Non-enzymatic electrochemical dopamine sensing probe based on hexagonal shape zinc-doped cobalt oxide (Zn-Co_2O_4) nanostructure. *Microchimica Acta*, 189:1-12, 2022.
39. Yu, D., Ma, Y., Chen, M. and Dong, X. KOH activation of wax gourd-derived carbon materials with high porosity and heteroatom content for aqueous or all-solid-state supercapacitors. *J. Colloid Interface Sci*., 537:569-578, 2019.
40. Du, W., Zhang, Z., Du, L., Fan, X., Shen, Z., Ren, X., Zhao, Y., Wei, C. and Wei, S. Designing synthesis of porous biomass carbon from wheat straw and the functionalizing application in flexible, all-solid-state supercapacitors. *J. Alloys Compd*., 797:1031-1040, 2019.
41. Sharma, M., Hussain, N., Mohanty, S., Puzari, P. and Deb, P. Robust energy storage performance enabled by the interacting interface of an epitaxial hybrid nanostructure based flexible supercapacitor. *J. Energy Storage*, 72:108345, 2023.
42. Jiang, L., Sheng, L., Chen, X., Wei, T. and Fan, Z. Construction of nitrogen-doped porous carbon buildings using interconnected ultra-small carbon nanosheets for ultra-high rate supercapacitors. *J. Mater. Chem. A*, 4(29):11388-11396, 2016.
43. Zhang, Y., Sun, Q., Xia, K., Han, B., Zhou, C., Gao, Q., Wang, H., Pu, S. and Wu, J. Facile synthesis of hierarchically porous N/P codoped carbon with simultaneously high-level heteroatom-doping and moderate porosity for high-performance supercapacitor electrodes. *ACS Sustainable Chem. Eng*., 7(6):5717-5726, 2019.

44. Tomar, A.K., Singh, G. and Sharma, R.K. Charge storage characteristics of mesoporous strontium titanate perovskite aqueous as well as flexible solid-state supercapacitor cell. *J. Power Sources*, 426:223-232, 2019.
45. He, J., Zhang, D., Wang, Y., Zhang, J., Yang, B., Shi, H., Wang, K. and Wang, Y. Biomass-derived porous carbons with tailored graphitization degree and pore size distribution for supercapacitors with ultra-high rate capability. *Appl. Surf. Sci*., 515:146020, 2020
46. Ma, T., Zhang, X. and Wang, Y. Tassel tree flowers-derived hierarchically porous carbons with high surface area for high-performance flexible all-solid-state symmetric supercapacitors. *J. Energy Storage*, 26:101014, 2019.
47. Shi, W., Chang, B., Yin, H., Zhang, S., Yang, B. and Dong, X. Crab shell-derived honeycomb-like graphitized hierarchically porous carbons for satisfactory rate performance of all-solid-state supercapacitors. *Sustainable Energy Fuels*, 3(5):1201-1214, 2019.
48. Mishra, S., Maurya, P.K. and Mishra, A.K. 2H–MoS_2 nanoflowers based high energy density solid state supercapacitor. *Mater. Chem. Phys*., 255:123551, 2020.